Cronfa - Swansea University Open Access Repository

_____

This is an author produced version of a paper published in :
New Journal of Physics

_____

Cronfa URL for this paper:

http://cronfa.swan.ac.uk/Record/cronfa20244

_____

Paper:

Bainbridge, A. & Bryan, W. (2014). Velocity map imaging of femtosecond laser induced photoelectron emission from metal nanotips. *New Journal of Physics, 16*(10), 103031

http://dx.doi.org/10.1088/1367-2630/16/10/103031

_____

Velocity map imaging of femtosecond laser induced photoelectron emission from metal nanotips

A R Bainbridge[1] and W A Bryan[1,2]

[1] Department of Physics, College of Science, Swansea University, Swansea SA2 8PP, UK
[2] STFC Central Laser Facility, Rutherford Appleton Laboratory, Harwell Oxford, Didcot OX11 0QX, UK
E-mail: w.a.bryan@swansea.ac.uk

Abstract

A novel application of velocity-map imaging (VMI) is demonstrated, whereby the momentum distribution of photoelectrons ejected from a tungsten nanoscale metal tip (<50 nm radius) is recorded following illumination with an ultrafast laser pulse. The electrostatic conditions in the VMI instrument are optimized through finite element modelling, taking into account a physically realistic geometry including all conductive elements in the vicinity of the electron trajectories. The instrument is calibrated by observing above threshold ionization in krypton gas, and simultaneous electron emission from this gas and a tungsten nanotip is presented, illustrating that the velocity mapping condition is maintained. Realizing photoelectron VMI for femtosecond laser illuminated nanoscale objects will have a significant impact on the emerging field of ultrafast nanoplasmonics and will influence the development of such devices as a source of coherent pulses of electrons with applications in time-resolved microscopy, holography and diffractive imaging.

Keywords: velocity map imaging, nanotip, tunnel ionization, ultrafast photoelectron spectroscopy

1. Introduction

Focusing an ultrafast laser pulse into an effusive or supersonic gas target generates a sufficiently strong electric field to initiate ionization and fragmentation. The initial state of the system is imprinted on the fragment electrons and ions modulated by the interaction with the laser pulse, hence the ability to measure the momentum of emitted particles allows inference of geometric and energetic characteristics [1, 2]. Such studies are highly informative, forming the foundation of a significant proportion of modern strong-field, synchrotron and free-electron laser research. Velocity map imaging (VMI) is a relatively simple yet powerful technique whereby the three-dimensional (3D) distribution of charged particle momenta is projected onto a two-dimensional detector by means of cylindrically symmetric electrostatic fields. Developed in 1997 by Eppink and Parker [3], VMI requires that the laser–target interaction take place in a region of high electric potential which directs charged fragments of a selected polarity towards a position sensitive detector, often a microchannel plate (MCP) and phosphor screen recorded with a CMOS or CCD camera.

The key consideration is that an electrostatic lens is formed along the path of the charged particle such that electrons or ions of a particular momentum arrive at the same point in the detector plane independent of the point of creation. It is relatively straightforward to have this condition apply over a large volume: a VMI apparatus of dimensions hundreds of millimetres will successfully momentum image over of the order of millimetres to tens of millimetres. This is of particular relevance to strong-field ultrafast laser dynamics, whereby a laser pulse is focused down to a beam waist on the order of microns, causing nonlinear processes such as tunnel ionization, recollision excitation and ionization, formation of rotational and vibrational wavepackets and molecular fragmentation. Furthermore, the dynamics of electronic wavepackets can be directly driven by manipulating the carrier-envelope phase (CEP) of the laser pulse if it is of a few optical cycles in duration [4, 5]. The laser spot size and Rayleigh length is often much smaller than the collection region of a VMI instrument, and if the laser pulse duration is picoseconds to few femtoseconds, dynamics relevant to gas-phase atomic and molecular systems become observable.

A number of adaptions of the traditional VMI design have been proposed, extending the resolution or improving the applicability to specific areas of ultrafast laser–matter interaction physics. Integrating the gas source into one of the electrodes increases the target gas density [6] allowing the low photon fluxes typically associated with high harmonic XUV, FEL or attosecond pulses to be accommodated [7–10]. Single-shot CEP-tagging has negated the need for CEP-stabilization through the use of fast imaging and processing techniques [11], and can potentially be applied to other laser parameters. Electrostatic adaptations on the traditional design use multiple or shaped electrodes, which can enhance focusing and thus increase energy resolution. Experimental observations coupled with modelling determined a relationship between the number of electrodes and the maximum achievable resolution [14] making it possible to systematically design extended VMI systems capable of operating at energy resolutions in the meV range.

In the present work, we look to demonstrate VMI of photoelectron emission from a metal nanotip illuminated with a strong field laser pulse, an area of active research worldwide [12, 13]. The radius of curvature at the tip of such objects (typically tens of nanometres) enhances the electric field induced by the incident radiation field [15–17], hence electron tunnelling into the continuum can be caused by very low fluences as compared to a gas phase

atomic or molecular target [18–22]. Such devices are attracting significant interest at the interface between ultrafast atomic physics, nanoscale plasmonics and electron microscopy. Similar sources are employed in transmission electron microscopy and low-electron energy point projection microscopy and holography [23–25], the latter having demonstrated that metal nanotips that come to a single atom point produce very highly coherent electron beams [26–30]. Atomic resolution has been demonstrated with such a source through the combination of holography and coherent diffractive imaging [31–33], though to date it has not been possible to combine this with femtosecond temporal resolution. The present work is motivated by the desire to extend our ability to characterize electron emission in the strong field regime, whereby ultrafast laser pulses are employed to generate coherent femtosecond electron pulses. An accurate understanding of the angular spread, absolute momentum and bandwidth of the electron pulses is vital for their application to time-resolved imaging via diffraction and microscopy [34].

2. Simulations

Introducing a conductive solid into the interaction region of a VMI spectrometer has a disruptive influence on the carefully balanced and rotationally symmetric electric fields. In the case of a gas phase atom, ejected electrons move under the action of the electrostatic potential at which they are created, and it is vital that the electron density is sufficiently low so as to avoid space-charge modification to the electron trajectories through the spectrometer. Once the atom or molecule has fragmented, it is replenished through gas flow into the vacuum chamber. When a solid conductor is used as a target, an electrical connection to an external source of current must be made so as to replenish charge ejected into the continuum. This current cannot flow without the conductor being held at a potential, which interacts directly with the field formed by the surrounding VMI electrodes.

The traditional configuration of a VMI uses three flat or cylindrically symmetric conical electrodes with large apertures some distance from a position sensitive detector, which generally also acts as a ground reference for the accelerating electrons. The gas source and laser focus are located between the repeller and extractor electrodes, and the third electrode then acts as a focusing device. The electric field gradient also directs electrons towards the detector. This is the simplest way of achieving the velocity mapping condition, and has been widely applied to ultrafast atomic physics and physical chemistry [1, 4]. With the additional requirement for placing a conductive solid at the laser focus, we adapt the multi-electrode design of Suzuki and co-workers [14], which makes use of a larger stack of multiple focusing electrodes to achieve higher resolution. By defining the electrostatic potential with more active electrodes, we aim to compensate for the influence of the nanotip target.

A schematic of the VMI instrument is shown in figure 1, which consists of eight electrodes, each separated by 22 mm. The aperture diameter is 50 mm at the interaction region, and increases to 75 mm towards the detector to accommodate the curved electron trajectories. The nanotip is mounted on an insulating arm placed between electrodes 1 and 2, with the remaining electrodes used to ensure correct focusing. Electrode 1 has a fine mesh applied to manage the field flatness at the interaction region. All electrodes are flat with a thickness of 1 mm and are held in place with insulating rods and ceramic spacers. In order to evaluate the effectiveness of the VMI design prior to construction, finite element modelling of the electric
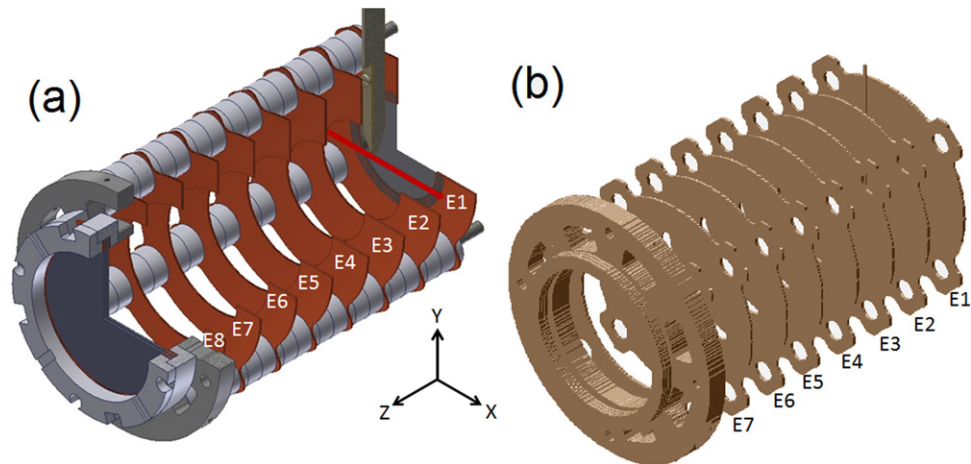
Figure 1. (a) Section view of the CAD model used for the simulations, including insulating components. (b) Actual SimION configuration imported from (a), showing all conducting components including electrodes, tip connection wire, mounting collar and detector electrodes. The 100 fs laser pulse propagates along *X* between E1 and E2 as shown in red, and is linearly polarized along *Y*.

field structure was performed using the model in figure 1(b), exported from Autodesk Inventor 2013 and imported into SimION 8.0.4, allowing real geometry and sizes to be used rather than relying on the typically rotationally symmetric approximations that are often used in such cases. With all insulating elements ignored and optimized potentials applied, SimION was used to calculate electron flight trajectories through the electrodes, and so allows any unwanted areas of localized field gradient to be quickly highlighted.

As an initial step, with the nanotip and contact wire removed from the SimION model, an optimization of the electrode voltages demonstrated the velocity mapping condition could readily be achieved with the eight electrode configuration detailed in figure 1. Optimization of the applied voltages on electrodes E1–E8 allowed focusing characteristics to be found, and demonstrates the ability of the eight-electrode stack to achieve velocity focusing for a variety of electron energies at realistically applicable voltages. As a test of the ability of the apparatus to velocity focus for a wide range of initial energies simultaneously, non-interacting electrons were simulated with kinetic energies of 2, 20, 30 and 40 eV and propagated to the detector plane as shown in figure 2. 1000 electrons at each of these energies were emitted from the centre of the interaction region over a filled sphere of 1 mm radius. The electron momentum vectors were defined by an opposing pair of 3D Gaussians centred on and rotationally symmetric about the *Y* axis to simulate the effect of linear laser polarization along that axis, albeit with an exaggerated FWHM of 75° to enhance the clarity of any defocusing effects, and ensure that the effect of focusing a specific energy to a specific radius is met over full rotational symmetry.

The results as displayed in figure 2 demonstrate that as we are projecting a 3D distribution of electrons onto a two dimensional detector, the narrow momentum width fringes become flattened spheres, albeit with hard edges. Each hard edge forms a circle to which each energy is focused, with smaller radius indicating lower energy. The inner area of the circles are partially and randomly filled by those electrons emitted at larger angles towards or away from the detector, a realistic effect of the rotational symmetry of the initial distribution. The initial
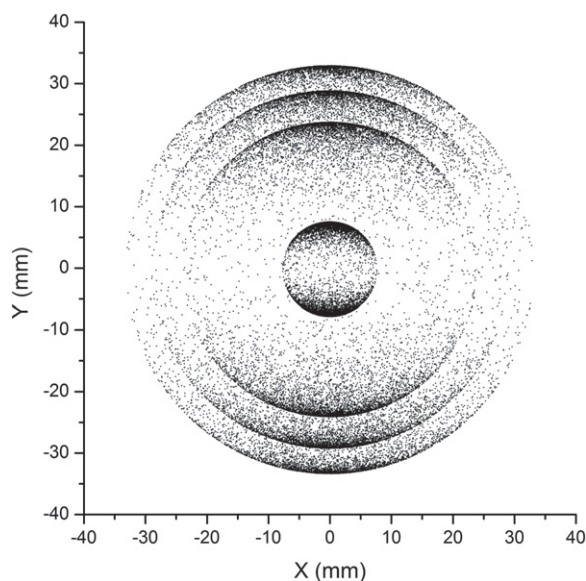
Figure 2. Simulation demonstrating ability of the multi-electrode VMI design to achieve simultaneous focusing of a variety of electron energies. The electrons originate at (0,0) in rotationally Gaussian distributions about the *y* axis, with discrete energy populations of 2, 20 30 and 40 eV. Electrons of the same energy are successfully focused onto the same radius.

angular distribution of the electrons is revealed by the extent to which the circumference of the circle is filled, in this case revealing that the majority of electrons are released along the *Y* axis.

With all elements (nanotip, supply wire, VMI electrodes, detector mounting collar, detector electrodes) defined with independent voltages, a systematic study of the VMI focusing conditions was performed. This investigated the effect of tip voltage and position on the parameters of the resulting focus. The simulation includes the added asymmetric potential caused by the presence of the tip and its contact wire, which was placed at realistic positions within the spectrometer by varying the distance between the tip and electrode 2, accounting for the limitations of the real geometry and testing the ability to momentum focus despite the freedom to move the tip. Electron flight through the spectrometer was then modelled for a range of tip voltages.

There are three approximations of note: (1) The initial electron distribution was modelled as a small sphere with zero energy. This replicates the observed strong-field behaviour of gas phase photoelectron emission, used as a diagnostic and discussed later.

(2) It was necessary to approximate the tip (and the connection wire) as a simple cylinder with a flat end, as SimION is incapable of dealing accurately with undulating geometries due to the lack of an adaptive grid, and was not able to accurately refine the taper of the tip into the grid due to the small size of the tip relative to the grid size. To use a grid size small enough would have rendered the simulations too computationally expensive for our current resources. We anticipate that the microscopic geometry of the tip and the resulting field will have an influence on the resulting velocity map distribution, and is an area of future investigation where we expect to see the structure of the VMI image reflecting the distribution of emission sites across the curvature of the tip. Investigation of the extent of this influence is ongoing.

(3) The negligence of space-charge is again due to the availability of computation resources, but is not an unreasonable approximation as it is possible to emit an average of the order of one electron per laser pulse from a tip with sufficiently low intensity. This is advantageous as by integrating over a large number of single electron shots it is possible to severely reduce or eliminate disruption caused by space charge [31]. Even when releasing multiple electrons per shot this approximation may still hold, as the large geometry of the VMI and the strong static fields present will naturally allow and encourage a large separation between electrons, where the field from the VMI will totally dominate space-charge effects. The area where this approximation becomes a real experimental issue is at the plane of the detector, as the simulation cannot account for the action of the MCP and the resulting coulomb expansion between the MCP and phosphor screen. This results in a simulated distribution that is accurate upon arrival at the detector but appears more tightly focused than the results observed on the screen due to spreading of the distribution within the detector. It is anticipated that accounting for mutual repulsion during the flight through the electrodes would lead to some smearing of the image upon arrival at the front of the detector, which would normally be sufficiently minor as to be unobservable in comparison to the smearing caused within the detector itself, only becoming a major problem upon the release of $\geqslant 10^5$ electrons per shot.

The results of this simulation are shown in figure 3. For a series of nanotip positions with respect to E2, the applied nanotip voltage Vtip was scanned through the velocity mapping focus, and 5000 electrons were flown individually through the VMI. The coordinates in the detector plane of all electrons were recorded and the mean and standard deviation in the detector plane (X and Y) used to quantify the parameters of the final focus.

Figure 3(a) shows the displacement, defined along the Y-axis, a measure of the deflection of the mean coordinate of the electron bunch from the center of the detector caused by the potential on the tip. Positive displacement is defined as away from the tip (indicated in figure 1). Only Y displacement is considered as for a symmetric nanotip and straight contact wire there should be very little X-axis displacement. As is clear from the shape of the curves in figure 3(a), it was found that the dependence of displacement on Vtip was remarkably independent of tip position, with only changing factor being the intersect with 0 which shifts by 21.5 ± 1 V mm^{-1} of tip translation for the given electrode voltages.

The spatial spread of electrons arriving at the detector plane (effectively the electron focal spot) is quantized by the standard deviation from the mean along both the X and Y axes. As shown in figure 3(b), the standard deviation along the X axis (σ_X) passes through a clear minimum which occurs at the same tip voltage (to within ±2 V) as the point of zero displacement shown in figure 3(a). Again the shape of the curve remains remarkably similar as the tip position is changed, with the voltage of best focus shifting again by 21.5 ± 1 V mm^{-1}. The spot size in the X dimension is also symmetric about the minimum, which remains constant as the tip is moved. The symmetry of this observation is a result of the additional axis of symmetry around the Z axis.

The most interesting prediction occurs when the electron spot standard deviation along the Y axis is considered. A minimum in the standard deviation along the Y axis (σ_Y) is observed, shown in figure 3(c), which occurs at approximately the same voltage as the minimum in X and the point of zero displacement, figures 3(a) and (b), however the function is highly asymmetric. When the tip voltage is too low such that a negative displacement occurs the defocusing of the spot is extremely rapid as it expands along the tip axis. The minimum, whilst clear, is less well defined and is predicted to be a factor of 35 larger on the Y axis than the X axis. When the tip
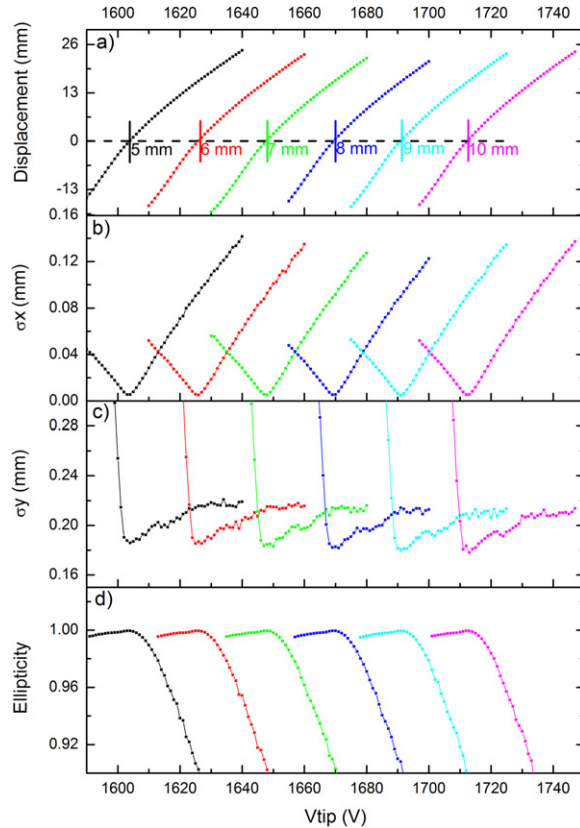
Figure 3. Results of simulation of electron flight through the VMI as a function of tip voltage and position. (a) Displacement of the center of the electron bunch from the center of the detector along Y. (b), (c) Standard deviation of the electron bunch along the detector in X and Y, respectively. (d) Predicted ellipticity of the bunch arriving at the detector. Tip positions are defined relative to E2 in the Z axis, and are chosen to reflect tip positions used in the real VMI, where the tip typically sits closer to E2 than E1 due to the geometry of the vacuum chamber.

voltage is above the required focusing voltage the defocusing occurs much less rapidly, expanding faster along the X axis than the Y axis. Fluctuations in the data in figure 3(c) is a result of small statistical variation in the simulation.

The measurement of spot size on the Y axis does not follow the same pattern as the X axis and displacement as the tip position changes. Although again the functions remain similar as the tip moves and the minima again shift by $21.5 \pm 1 \, \mathrm{V \, mm^{-1}}$, the value of the minimum point shifts slightly lower as the tip moves further away from the detector. This effect shows that it is advantageous to have the tip far from electrode 2. It was not possible to fully utilize this for the initial measurements presented below due to the geometry of the vacuum chamber, which requires that the tip is closer to electrode 2 than 1.

Whilst there is a predicted variation in the resolution in the X and Y directions, it is anticipated that this will not be an experimental limitation. The smallest σ_X is predicted to be of the order of $10 \, \mu\mathrm{m}$, resolution of which is not achievable with MCP and phosphor screen combination. The pore size of the current detector is $25 \, \mu\mathrm{m}$ with a separation of $32 \, \mu\mathrm{m}$, hence
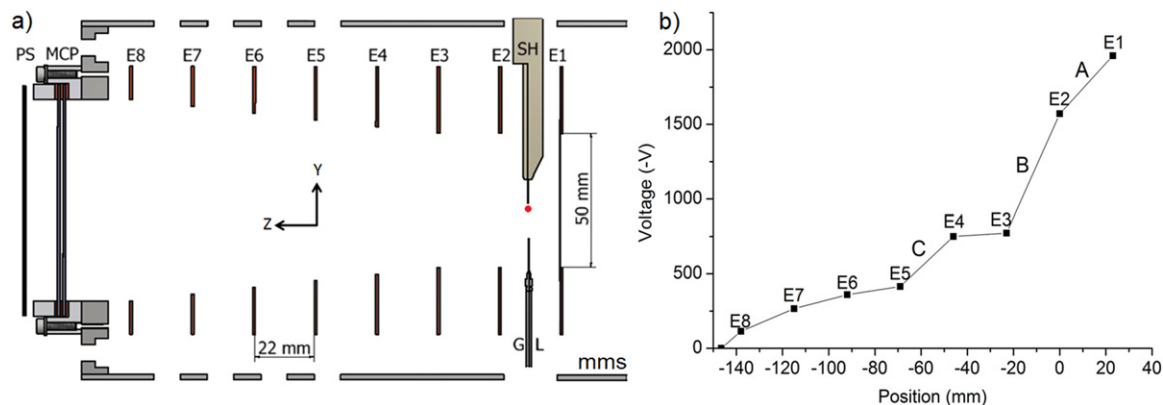
Figure 4. (a) Slice view schematic of the VMI spectrometer. The interaction region lies between electrodes E1 and E2, with the laser propagating perpendicular to the image plane as denoted by the red dot. The sample holder (SH) holds the tip electrically isolated from the rest of the chamber on a three-axis translation stage, and can be retracted for gas phase operation. A wire contained within the holder connects the tip to an external power supply. The gas line (GL) is held electrically floating and stationary. E3 retains a 50 mm inner diameter and is used for focusing, whilst E4 through E8 have an expanding inner diameter in 5 mm steps to 75 mm and are used to further refine the focusing and enhance resolution. The entire stack is enclosed in a grounded mu-metal shield (MMS) with pumping holes. (b) Typical electric potential of the VMI as a function of position. The zero point coincides with E2, the dots coincide with the electrode positions. Region A is the extraction area, where the sample must be kept at a potential that sits close to the line in order to avoid field disruption. Region B is the focusing region of a traditional VMI and reprises the same role in this adaptation. The remaining electrodes provide further focusing, with region C being a second major lensing area.

achieving a spot on the phosphor with a diameter comparable to the predicted minimum of σ_Y (approximately 200 μm) seems reasonable.

3. Apparatus

The VMI electrodes were manufactured from 1 mm thick OFHC copper, and are mounted on four rigid insulating PEEK rods. The electrode spacing and location is defined with standard male and female ceramic spacers. Two 86 mm diameter imaging MCPs are mounted at the end of the electrode stack, and following multiplication, imaged using a Kimball Physics P22 UHV phosphor screen with a 60 μs delay time. A schematic of this apparatus is shown in figure 4(a), and also indicates the position of the effusive gas line connected to a VG Scienta ZLVM940 leak valve, and the PEEK nanotip mount. The VMI assembly is encapsulated in a grounded mu-metal shield to prevent external electromagnetic fields from affecting electron flight, and the VMI + MCP assembly is mounted in a UHV chamber that typically operates at a base pressure of 10^{-9} mbar. Emission from the phosphor is monitored on an AVT Pike F-505 CCD camera (14 bit, 2452 x 2054 pixels) fitted with a Pentax C30811 8.5 mm f/1.5 2/3″ lens.

Potentials on the electrodes are applied by an eight-channel adjustable high voltage power supply; in practice it is rarely necessary to exceed 2 kV unless attempting to focus electrons with energies greater than 20 eV. Typical operating potentials are shown in figure 4(b): it should be

noted these voltages were the outcome of the SimION modelling, and were found to give excellent electron focusing. The voltage is applied near the outer edge of the electrodes to avoid the potential on the connection wires interfering with the symmetry of the electric fields.

The nanotips employed are electrochemically etched [35] from $250\,\mu$m diameter polycrystalline tungsten wire, achieving a radius of curvature below $100\,$nm as inferred by Fowler–Nordheim measurements [36]. The nanotips are etched, rinsed with ethanol then rinsed with deionized water before mounting. A PEEK clamp is used, giving good mechanical rigidity, minimal surface charging, easy machining and clearly a high dielectric strength. With the nanotip held in the clamp, a $100\,\mu$m gold wire is wrapped around the tip shaft, and connected to a kapton feedthrough wire. It was found that maintaining the gold connection wire as straight as possible minimized arcing and kept the electrostatic field as uniform as possible, as judged from calibration measurements.

Gas may be delivered into the system by means of the gas line shown in figure 4(a). It was found that using a metal gas needle that is grounded to the rest of the chamber creates significant disruption and can prevent proper focusing. To prevent this the needle incorporates a ceramic break outside the magnetic shield, leaving all components near the interaction region electrically floating.

4. Gas-phase calibration

Before characterizing the momentum distribution of photoelectrons from a solid nanotip target it is necessary to calibrate the spectrometer, done here by recording a momentum image of electrons emitted from krypton. High purity Kr is introduced into the interaction region through a $200\,\mu$m capillary mounted on the gas line, with the end of the capillary approximately $6\,$mm from the laser focus. The pressure in the chamber as measured with a Bayard-Alpert gauge increases to 4×10^{-7} mbar, with an estimated number density at the laser focus of $3 \times 10^9\,\mathrm{cm}^{-3}$.

Laser pulses from a Coherent Libra ($800\,$nm, $0.23\,$mJ, $105\,$fs @ $1\,$kHz) are transmission focused with a $f = 250\,$mm fused silica lens to a spot size of $40\,\mu$m full-width at base. At the focus, we estimate the peak laser intensity is just below $10^{14}\,\mathrm{W\,cm}^{-2}$, sufficient to initiate above-threshold ionization (ATI), whereby an atom simultaneously absorbs an excess of energy from the laser field, which is released as an electron with kinetic energy peaks separated by the photon energy [37]. The gas pressure, laser intensity and MCP gain is adjusted to produce the clearest ATI fringes on the phosphor screen. Importantly, we confirmed the SimION results by making small adjustments to the voltages applied to the eight electrodes, and found that the predicted values agreed with the best experimental resolution to within a volt. The figure of merit of VMI was the circularity, peak brightness and central position of the zero momentum emission from Kr.

An example velocity map of ATI in Kr is shown in figure 5(a), and shows electron emission strongly peaked along the laser polarization direction as anticipated. While a little blurred, it is possible to identify ATI fringes, facilitating momentum calibration to camera pixel. This blurring is the result of two influences: the gas is effusive, so near room temperature. Secondly, in this proof-of-principle experiment, the distance between the back of the MCP and the phosphor screen was approximately $13\,$mm, which caused a significant spreading of the electron cloud. In future designs, this will be reduced to around $2\,$mm, massively increasing the momentum resolution.
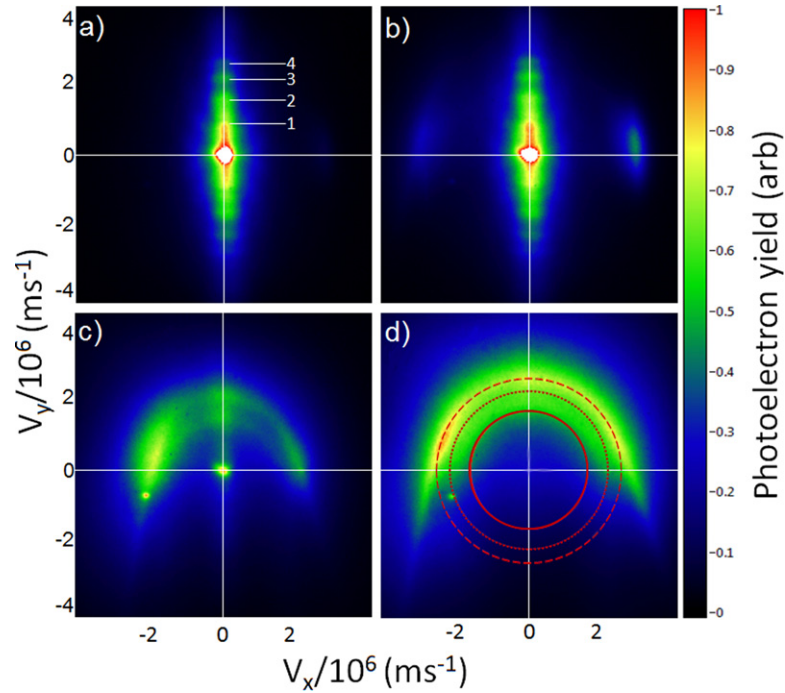
Figure 5. Colour enhanced images of real VMI patterns obtained with the apparatus from figure 4. In all images the tip is oriented along *Y*. Laser propagation is along *X*, with linear polarization along *Y*. (a) Image of krypton gas with ridges showing ATI. The marker numbers *n* indicate the position of *n*-photon emission. (b) Electrons present from both gas and nanotip, with tip at edge of beam. (c) Electrons from both gas and nanotip, with beam attenuated to allow tip signal to be highlighted. Some smearing is visible due to a sub-optimal Vtip. (d) Image of electron emission from nanotip only. The inner ring shows the lowest momentum where electrons were detected, followed by rings indicating the second (dotted) and third (dashed) photon energies as calibrated from the ATI ridges in (b). The off-center bright spot on (c) and (d) is a result of contamination on the MCP.

5. VMI of photoelectron emission from a solid nanoscale metal tip

The nanotip, held in the PEEK clamp is mounted on a three axis translation stage to freely allow the sample to be positioned relative to the laser focus. The rod must be made of an insulator extending at least as far as the mu-metal shield; it was found that using a rod with grounded metal components present within the boundary of the electrodes causes significant disruption to the focusing and can pull electrons along the *Y* axis. It should be noted that there is certainly a limit to the size of solid target that may be used. This limit is as yet undetermined, but it should be made as thin as possible along the *Z* axis to minimize disruption to the extraction and focusing fields, which may lead to loss of focus along the *Y* axis.

Examples of VMI images as the tungsten nanotip is moved into the laser focus are shown in figure 5(b). To demonstrate that we maintain velocity mapping conditions, the nanotip was very carefully inserted into the low intensity wing of the laser focus while we were generating ATI signal from Kr. A small lateral shift of the zero momentum point is observed, however this can be corrected by adjusting the tip voltage. Once we observed electron emission from the nanotip, the laser intensity was lowered by a factor of three. This is clearly necessary for three

reasons: the field enhancement caused by the nanotip is anticipated to increase the effective intensity by around an order of magnitude. The density of the nanotip is also many orders higher than the gas, and the ionization potential of tungsten is 6 eV lower than Kr. The combination of these effects means that exposing the tip to such an intensity would immediately generate a plasma, evaporating the tip.

With a laser pulse energy of $70\,\mu$J and the nanotip advanced around 100 microns into the focus, we simultaneously observe the zero momentum electrons from ATI of Kr at an estimated intensity of $8 \times 10^{12}\,\mathrm{W\,cm^{-2}}$ and electrons from the nanotip at an intensity of $\simeq 10^{11}\,\mathrm{W\,cm^{-2}}$. The electrons from the tip typically form a semicircular band on the detector, as shown in figure 5, suggesting an initial conical direction distribution centred along the tip (Y) axis, and a reasonably consistent energy across the entire distribution. By rotating the laser polarization, we confirmed the zero momentum spot was essentially unchanged, while the emission from the nanotip switched off. This is an important result from the present work: the two modes of operation are not mutually exclusive, and that it is possible to emit electrons from a solid target whilst also observing electrons from a calibration gas in order to adjust the focusing voltages in real time. This only requires the solid target to be smaller than the laser focus, and can be performed without any temperature control of the target or gas.

The laser pulse energy is then reduced to the nanojoule scale and the nanotip positioned approximately ten μm from the center of the focus. The corresponding electron VMI image is shown in figure 5(d). A clear signature of strong field emission is then observed: an almost semi-circular band of electron momentum centred at the zero momentum point. Identification of this structure as having a strong field origin comes through agreement with previous work [12, 38], which indicated that the majority of electrons emitted from a nanotip via the strong field regime have a specific and narrow energy spectrum. The emission process as compared between an atom and a nanotip has a number of similarities, however we do not expect zero momentum emission from a tip. The dominant band of electron emission is almost symmetric around the Y axis, indicating the surface enhancement effect is having a clear influence on ionization. We also observe a hotspot of electron emission in the direction that the laser pulse arrives from which is most likely due in part to thermionic emission. In future experiments, the size of the focal volume will be reduced significantly, which will allow the nanotip to be placed at the focus without illuminating the shank. It is this that produces thermionic emission, rather than from the tip apex, and can readily blunt a nanotip. This is confirmed through destructive testing where the tip is moved further into the VMI such that it blocks a significant portion of the exit beam. This causes the semicircular band structure to by suppressed and the thermionic feature to become dominant, forming a much broader momentum distribution with no discernible internal structure other than a distribution that is approximately Boltzmann-like. Returning the tip to its original position reduces the thermionic component but generally yields a significantly modified and weaker strong field emission structure, or none at all. This is indicative of the thermionic electrons being emitted during a one-way evaporation or heating process that permanently alters the tip shape.

The simulations predict a very high ellipticity at the point of best focus due to the spot size in the X axis being dramatically smaller than in the Y axis. This suggests that the point needs to be both large and at high displacement in order to achieve a round spot from a spherical distribution. In this aspect the simulations disagree from our observations, which showed that with careful handling of the tip position and voltage it is possible to obtain a circular spot at low displacement and with usable focusing of both the spot and ATI fringes. We anticipate this is

due in part to the effect of the MCP's spreading the electron distribution before arrival at the phosphor screen, and will be modified in future experiments. Furthermore, as shown in figure 5(d), we expect little zero momentum signal from the nanotip. Electrons with a non-zero momentum will spend significantly less time in the vicinity of the tip, so their trajectories may be influenced to a lesser degree, resulting in less disruption to the maximum achievable resolution. Experimentally there are strong indications when the correct VMI conditions are found. It was observed that when the tip voltage was too low the zero momentum distribution expanded rapidly towards the tip along the tip axis, replicating the steep gradient seen in figure 3. It was also observed that at increasing tip voltage the distribution expanded more rapidly in the axis perpendicular to the tip, again replicating the prediction of the simulation.

6. Conclusion and discussion

We have presented a novel adaptation to the traditional VMI spectrometer design that allows simultaneous observation of the momentum distribution of photoelectrons from gas and solid targets. The effectiveness of this revised design has been demonstrated by examining above threshold ionization from krypton gas and tunnelling emission from a tungsten nanotip. Conditions are found that allow photoelectrons from the tip to be observed whilst using the structure of the zero-momentum spot from Kr to verify velocity focusing. This capability allows easy calibration of electrons emitted from a solid by comparison to those emitted from a noble gas under the same velocity focusing conditions.

The agreement between the SimION predicted VMI focusing conditions and the appearance of the symmetric structure in the observed distribution demonstrates that the instrument is operating in the velocity mapping regime, however it is well known that the enhancement of both DC and laser fields has a dominant influence over hundreds of nanometres, a smaller length scale than is possible to simulate with SimION. These simulations show that it is possible to maintain the VMI conditions over a wide range of configurations, crucially it is possible to retain the condition that the focusing is independent of the emission location. When moving the tip closer to or further away from the detector it is possible to restore a velocity focusing condition only by adjusting the potential applied to the tip for a given set of electrode voltages, whilst returning to a focus of very similar parameters. Such a condition could be very influential if this instrument is employed for examining overlapping laser foci, as will be required in pump-probe experiments.

Finally, this instrument gives direct access to 3D emission characteristics from metal nanotips illuminated with femtosecond laser pulses. Knowledge of the momentum distribution will be decisive in the design of next-generation femtosecond electron diffraction and microscopy instruments. Furthermore, this knowledge may be combined with state-of-the-art codes such as GPT [39] and SuperFish, permitting simulation of small geometries using adaptive grids, which will increase our understanding of the enhancement effects.

Acknowledgements

References

[1] Whitaker B J 2003 *Imaging in Molecular Dynamics* (Cambridge: Cambridge University Press)
[2] Tsubouchi M, Whitaker B J, wang L, Kohguchi H and Suzuki T 2001 *Phys. Rev. Lett.* **86** 20
[3] Eppink A T J B and Parker D H 1997 *Rev. Sci. Instrum.* **68** 9
[4] Carley R E, Heesel E and Fielding H H 2005 *Chem. Soc. Rev.* **34** 949–69
[5] Minns R S, Patel R, Verlet J R R and Fielding H H 2003 *Phys. Rev. Lett.* **91** 243601
[6] Ghafur O, Siu W, Johnsson P, Kling M F, Drescher M and Vrakking M J J 2009 *Rev. Sci. Instrum.* **80** 033110
[7] O'Keeffe P *et al* 2011 *Nucl. Instrum. Methods* B **284** 69–73
[8] O'Keeffe P, Bolognesi P, Coreno M, Moise A, Richter R *et al* 2011 *Rev. Sci. Instrum.* **82** 033109
[9] Remetter T *et al* 2006 *Nat. Phys.* **2** 323
[10] Johnsson P, Siu W, Gijsbertsen A, Verhoeven J, Meijer A S, Van der Zande W and Vrakking M J J 2008 *J. Mod. Opt* **55** 2693
[11] Säßmann F *et al* 2011 *Rev. Sci. Instrum.* **82** 093109
[12] Krüger M, Schenk M and Hommelhoff P 2011 *Nature* **475** 78
[13] Breuer J and Hommelhoff P 2013 *Phys. Rev. Lett.* **111** 134803
[14] Liu S-Y, Alnama K, Matsumoto J, Nishizawa K, Kohguchi H, Lee Y-P and Suzuk T 2011 *J. Phys. Chem.* A **115** 2953–65
[15] Yalunin S, Herink G, Solli D R, Krüger M, Hommelhoff P, Diehn M, Munk A and Ropers C 2012 *Ann. Phys.* **525** 12–18
[16] Yanigasawa H 2012 *Ann. Phys.* **525** 126–34
[17] Park D J, Piglosiewicz B, Schmidt S, Kollmann H, Mascheck M, Groß P and Lienau C 2012 *Ann. Phys.* **525** 135–42
[18] Herink G, Solli D R, Gulde M and Ropers C 2012 *Nature* **483** 190
[19] Krüger M, Schenk M, Förster M and Hommelhoff P 2012 *J. Phys. B: At. Mol. Opt. Phys.* **45** 074006
[20] Schenk M, Krüger M and Hommelhoff P 2010 *Phys. Rev. Lett.* **105** 257601
[21] Hommelhoff P, Sortais Y, Aghajani-Talesh A and Kasevich M A 2006 *Phys. Rev. Lett.* **96** 077401
[22] Barwick B, Corder C, Strohaber J, Chandler-Smith N, Uiterwaal C and Batelaan H 2007 *New. J. Phys.* **9** 142
[23] Quinonez E, Handali J and Barwick B 2013 *Rev. Sci. Instrum.* **84** 103710
[24] Latychevskaia T, Longchamp J-N and Fink H-W 2012 *Opt. Express* **20** 28871
[25] Longchamp J-N, Latychevskaia T, Escher C and Fink H-W 2013 *Phys. Rev. Lett.* **110** 255501
[26] Paarmann A *et al* 2012 *J. Appl. Phys.* **112** 113109
[27] Ropers C, Solli D R, Schultz C P, Lienau C and Elsaesser T 2007 *Phys. Rev. Lett.* **98** 043907
[28] Mutus J Y, Livadaru L, Urban R, Pitters J, Legg A P, Salomons M H, Cloutier M and Wolkow R A 2013 *New. J. Phys.* **15** 073038
[29] Barwick B, Park H S, Kwon O H, Baskin J S and Zewail A H 2008 *Science* **322** 1227–3
[30] Cho B, Ichimura T, Shimizu R and Oshima C 2004 *Phys. Rev. Lett.* **92** 246103
[31] Sciaini C and Miller R J D 2011 *Rep. Prog. Phys.* **74** 096101
[32] Zewail A H and Thomas J M 2010 *4D Electron Microscopy: Imaging in Space and Time* (London: Imperial College Press)
[33] Gahlmann A, Tae Park S and Zewail A H 2008 *Phys. Chem. Chem. Phys.* **10** 2894–909
[34] Blaga C I, Xu J, DiChiara A D, Sistrunk E, Zhang K, Agostini P, Miller T A, DiMauro L F and Lin C D 2012 *Nature* **483** 194
[35] Melmed A J 1991 *J. Vac. Sci. Technol.* B **9** 601
[36] Fowler R H and Nordheim L 1928 *Proc. R. Soc.* A **119** 173–81

[37] Agostini P, Fabre F, Mainfray G, Petite G and Rahman N K 1979 *Phys. Rev. Lett.* **42** 1127
[38] Park D J, Piglosiewicz B, Schmidt S, Kollmann H, Mascheck M and Lienau C 2012 *Phys. Rev. Lett.* **109** 244803
[39] www.pulsar.nl/gpt